

Evaluating geodynamic models for sub-slab anisotropy: Effects of olivine fabric type

Colton Lynner^{1,*}, Maureen D. Long¹, Christopher J. Thissen², Karen Paczkowski^{1,3}, and Laurent G.J. Montési³

¹Department of Geology & Geophysics, Yale University, New Haven, Connecticut 06520, USA

²Department of Terrestrial Magnetism, Carnegie Institution for Science, Washington, D.C. 20015, USA

³Department of Geology, University of Maryland, College Park, Maryland 20742, USA

ABSTRACT

We examine spatially varying patterns of sub-slab anisotropy derived from geodynamic models of subduction beneath Central America and Tonga. Invoking a variety of anisotropic fabrics, we compare the predicted sub-slab anisotropy of these models against source-side, shear-wave splitting observations using realistic ray paths. We find that in both regions fabric type has a strong impact on predicted shear-wave splitting. In Tonga, where three-dimensional (3D) return flow dominates, E-type olivine lattice-preferred orientation (LPO) fabric predicts a sub-slab mantle anisotropy that best matches observations. In Central America, where entrained flow dominates, anisotropy from C-type LPO fabric yields the best fit. This highlights the importance of fabric type when interrogating geodynamic models because different regions may be characterized by different LPO fabrics. A primary controller of fabric type is water content. Taken at face value, these results then suggest the sub-slab mantle beneath Tonga is less well hydrated than that beneath Central America.

1. INTRODUCTION

In the past few years, there has been a concerted effort to constrain seismic anisotropy beneath subducting slabs, primarily through the use of shear-wave splitting (e.g., Müller et al., 2008; Long and Silver, 2009; Abt et al., 2010; Di Leo et al., 2014; Lynner and Long, 2013, 2014a, 2015). Shear-wave splitting is a powerful tool that has been employed in a variety of regions to measure seismic anisotropy (see reviews by Savage, 1999; Crampin and Peacock, 2008; Long, 2013). A detailed understanding of seismic anisotropy can shed light on various aspects of mantle behavior, including patterns of mantle flow and conditions of deformation, such as stress, temperature, and hydration state.

Seismic anisotropy in the upper mantle is typically attributed to the aligned axes of olivine, a seismically anisotropic mineral (Karato et al., 2008). A non-random arrangement of mineral axes is called lattice-preferred orientation (LPO). Under dislocation creep, olivine LPOs are generated by the rotation

*Current address: Department of Geosciences, University of Arizona, Tucson, Arizona 85721, USA

of mineral axes relative to the deformation geometry. The local stress, temperature, and water content during deformation determine the relationship between LPO orientation and deformation geometry (Karato et al., 2008).

Given constraints on the deformation conditions in the sub-slab mantle, the most likely LPO fabrics are A-type, C-type, and E-type (see Karato [2012] for in-depth discussion of LPO development conditions). Each of these LPO fabrics is characterized by a general relationship between finite strain and anisotropy where the orientation of the seismically fast axis for vertically propagating shear waves closely aligns with the orientation of maximum extensional strain. For non-vertically propagating waves, such as direct teleseismic S waves used in source-side splitting, different olivine LPO fabrics predict highly variable shear-wave splitting observations (Fig. 1). This variability has implications for inferring deformation geometry in the upper mantle. The sensitivity of the seismic observations to olivine fabric type also provides a potential mechanism for determining the stress, temperature, and water conditions in the upper mantle.

Source-side, shear-wave splitting observations can provide the coverage in initial polarization and incidence angle needed to distinguish among the different olivine LPO fabric types. The source-side, shear-wave splitting technique uses earthquakes and distant seismic stations (40° to 80° apart in epicentral distance) to probe anisotropy beneath seismic sources. The source-side anisotropic signal can be isolated once the anisotropy beneath the seismic stations has been removed (for an in-depth discussion of practical considerations for source-side splitting measurements, see Lynner and Long [2014a]). Source-side splitting is particularly powerful in subduction zones due to abundant slab seismicity. It not only provides a depth constraint on anisotropy but can easily sample the sub-slab mantle. A recent semi-global compilation of source-side splitting beneath subducting slabs yielded both trench-parallel (e.g., beneath Tonga) and plate-motion-parallel (e.g., beneath Central America), fast-splitting directions (Lynner and Long, 2014a).

Several conceptual models have been proposed to explain trench-parallel, fast-splitting directions beneath subducting slabs (Fig. 2). The 3D return flow model (Russo and Silver, 1994; Long and Silver, 2008, 2009) suggests that subducting slabs undergoing trench rollback induce 3D-return flow around slab edges. Three-dimensional return flow contains a component of along-strike flow beneath the slab and thus yields anisotropy parallel to trench strike.

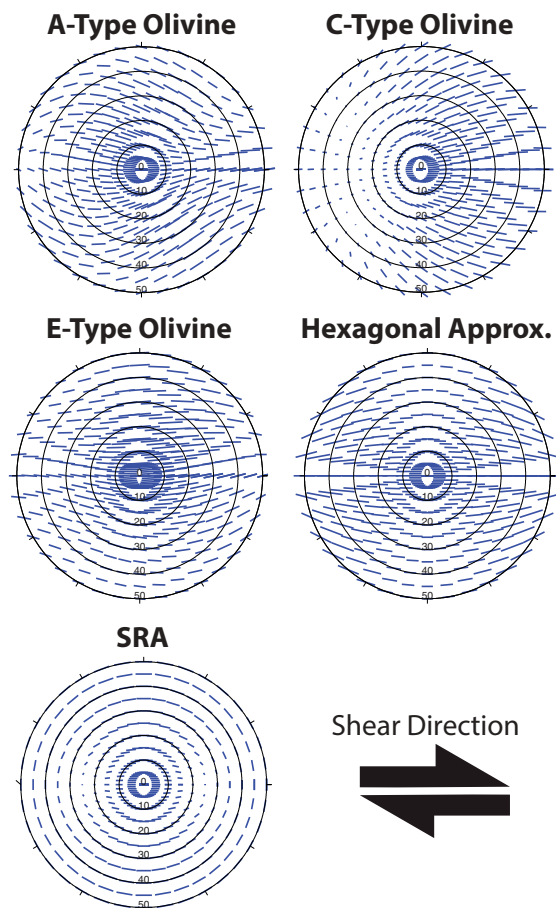


Figure 1. Splitting predictions (blue bars) for the five anisotropic fabrics considered here as a function of ray-propagation angle and event-to-station azimuth. The orientation of the bars corresponds to fast direction, and the length of the bars corresponds to delay time. The distance from the center of the plot represents the propagation angle of the ray (from the horizontal), and the azimuth corresponds to the event-to-station azimuth relative to the shear direction, assumed to be horizontal. Each plot is aligned such that the shear direction is to the right, and the shear plane normal direction is normal to the page. SRA—strong radial anisotropy model.

More recently, Song and Kawakatsu (2012, 2013) proposed that the sub-slab mantle is characterized by both azimuthal and a strong component of radial anisotropy; we call this the strong radial anisotropy model (SRA). This model suggests the sub-slab mantle is characterized by 2D entrained flow, and as the dip of the slab increases, the relative impact on shear-wave splitting of the azimuthal versus radial components of anisotropy changes. Once the radial component of anisotropy becomes stronger than the azimuthal component,

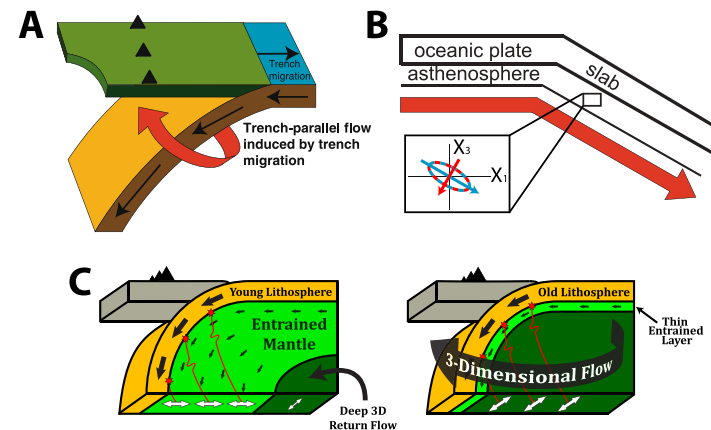


Figure 2. Conceptual diagrams of the (A) 3D return-flow model (after figure 4 from Long and Silver, 2008); (B) the strong radial anisotropy model (after figure 2 from Song and Kawakatsu, 2012); and (C) the age-dependent model (after figure 10 from Lynner and Long, 2014b), which incorporates an age-dependent transition from 2D entrained flow to 3D return flow.

trench-parallel fast directions are predicted despite the presence of simple 2D flow. The age-dependent model of Lynner and Long (2014b) proposes a change in sub-slab dynamics with the age of the downgoing lithosphere, where 2D entrained flow dominates beneath younger (<95 Ma) subducting slabs, and 3D return flow dominates beneath older (>95 Ma) subducting slabs. The likely cause of the transition between entrained dynamics and 3D return flow is a change in coupling between slabs and the subjacent mantle, possibly due to the onset of small-scale convection (e.g., Korenaga and Jordan, 2003; van Hunen and Čadek, 2009) or variable hydration state of the mantle (e.g., Olugboji et al., 2013).

In our previous work (Lynner and Long, 2014b), we used a semi-global compilation of source-side splitting measurements (Lynner and Long, 2014a) to test these three conceptual models. We compared the source-side splitting measurements with predictions of splitting calculated using realistic values for local slab dip and trench strike, ray incidence and azimuth, convergence direction, either a hexagonal olivine LPO approximation (Chevrot and van der Hilst, 2003) or the SRA (Song and Kawakatsu, 2012) fabric, and a simplified approximation of sub-slab flow (either entirely 2D entrained flow or flow entirely along strike). This study concluded that the age-dependent model best fit the data.

The sub-slab dynamics used in this previous study are, however, significant simplifications. To test conceptual models that predict 3D return flow (in the 3D return flow model or beneath old slabs in the age-dependent model), we assumed that the anisotropic symmetry axis was always parallel to the trench. In reality, 3D return flow involves a highly complex, spatially varying flow field, where only a component of the flow is trench-parallel. It is therefore necessary to examine splitting predictions for realistic, 3D

geodynamic models in order to assess the validity of the simplified anisotropic geometries employed by Lynner and Long (2014b).

A number of 3D numerical modeling studies have aimed at understanding sub-slab dynamics (e.g., Kneller and van Keken, 2007; Jadamec and Billen, 2010; Faccenda and Capitanio, 2012, 2013; Di Leo et al., 2014; Li et al., 2014; Paczkowski et al., 2014a). These studies have shown a variety of sub-slab flow regimes, including combinations of 3D return flow and entrained flow (e.g., Faccenda and Capitanio, 2012, 2013) and flow fields that vary both spatially (e.g., Paczkowski et al., 2014a) and temporally (Di Leo et al., 2014). A difficulty in evaluating the predictions of different geodynamic models against seismic observations lies in realistically translating model velocity fields into predictions of shear-wave splitting. A useful way to compare model results with shear-wave splitting observations is through the comparison of finite strain ellipsoids (FSEs) with fast-splitting directions (e.g., Di Leo et al., 2014; Li et al., 2014; Paczkowski et al., 2014b). This can be problematic, however, because different anisotropic fabrics result in subtle but important differences in predicted shear-wave splitting for identical FSEs. Several possible fabric scenarios may be present in the sub-slab mantle, including the range of olivine fabric types outlined above, and the SRA fabric of Song and Kawakatsu (2012, 2013).

In this study, we use realistic flow geometries derived from 3D numerical models, and we consider a range of elasticity tensors that correspond to different fabric scenarios to improve on the comparisons between sub-slab anisotropy model predictions and the splitting observations presented in Lynner and Long (2014a). Specifically, we consider A-, C-, and E-type olivine LPO fabrics, the SRA fabric (Song and Kawakatsu, 2012, 2013), and the hexagonal olivine approximation LPO fabric (Chevrot and van der Hilst, 2003). We use a set of previously published steady-state numerical sub-slab flow models for the Tonga and Central America subduction zones (Paczkowski et al., 2014a). These two regions were chosen for their relatively simple slab geometries and kinematics, as well as their relatively simple sub-slab, shear-wave-splitting behavior. For each combination of flow model and elasticity tensor, we compute shear-wave splitting parameters for a set of ray paths identical to those measured by Foley and Long (2011) for Tonga and Lynner and Long (2014a) for Central America.

2. BACKGROUND

2.1 LPO Fabric Development and Choice of Elasticity Tensors

Mineral physics experiments performed on polycrystalline olivine aggregates have shown that a variety of olivine LPO fabrics contribute to the anisotropy of the upper mantle in various geodynamic settings. A-type, C-type, and E-type fabrics are the most likely to be present in the sub-slab mantle, given the likely deformation conditions (Karato et al., 2008). All three fabrics are generally characterized by fast-splitting directions that roughly parallel

maximum extensional strain for the case of horizontal shear and vertically propagating waves. However, the three fabrics show pronounced differences in the details of their splitting patterns over a range of incidence angles and azimuths (Jung et al., 2006) (Fig. 1). A primary control on fabric development (A-, C-, or E-type) is water content in the mantle. A-type fabric develops at particularly low water contents (<~200 ppm H/Si), E-type develops in moderately hydrated mantle (between ~200 ppm H/Si and ~700 ppm H/Si), and C-type develops in well-hydrated mantle (>~700 ppm H/Si). The dominant fabric types may therefore vary spatially depending on the hydration state of the mantle (Karato et al., 2008; Michibayashi et al., 2016). In this study, we use elasticity tensors from the work of Jung et al. (2006) to represent A-, C-, and E-type fabrics. These tensors were obtained from experimentally determined polycrystalline fabrics and single-crystal olivine elasticity via a Voigt-Reuss-Hill averaging scheme.

The SRA elastic tensor comes from the work of Song and Kawakatsu (2012). The elasticity tensor was determined by combining components of azimuthal (2% azimuthal anisotropy) and radial anisotropy (3% radial anisotropy) to obtain an elastic tensor with an orthorhombic symmetry that could match seismic observations. The elastic tensor for the hexagonal olivine LPO fabric was taken from Chevrot and van der Hilst (2003). This tensor was obtained by mixing the average elastic olivine tensor of Kumazawa and Anderson (1969) around the crystallographic *a*-axis with an isotropic reference.

2.2 Geodynamic Modeling

Paczkowski et al. (2014a, 2014b) solved for the 3D steady-state mantle flow field beneath subduction zones using the COMSOL Multiphysics® finite element modeling software. The models consider an incompressible, isoviscous, Newtonian fluid. Although the slabs in these models remain planar, efforts were made to approximate other characteristics of specific subduction systems. In particular, the models include appropriate values of slab dip and maximum slab penetration depth from Lallemand et al. (2005), regional mantle flow and plate motions from Conrad and Behn (2010), and trench migration rates from DeMets et al. (1994) and Schellart et al. (2008). The thickness of the upper mantle and the width of the slab in each model were set to ~670 km and ~1000 km, respectively (Fig. 3). An important distinction made in each model is the depth to which the subducting slab penetrates into the mantle. Another important modeling choice is whether the downgoing slab and sub-slab mantle are coupled or decoupled. The optimal sub-slab coupling condition was determined by Paczkowski et al. (2014b) through a comparison of predicted FSEs and observed fast-splitting orientations. In both Tonga and Central America, however, differences between coupled and non-coupled models are minimal (Figs. 3C and 3D); therefore, the choice of coupling condition is not a major factor. In all models, flow surrounding the slab is driven by a combination of slab kinematics and background mantle flow.

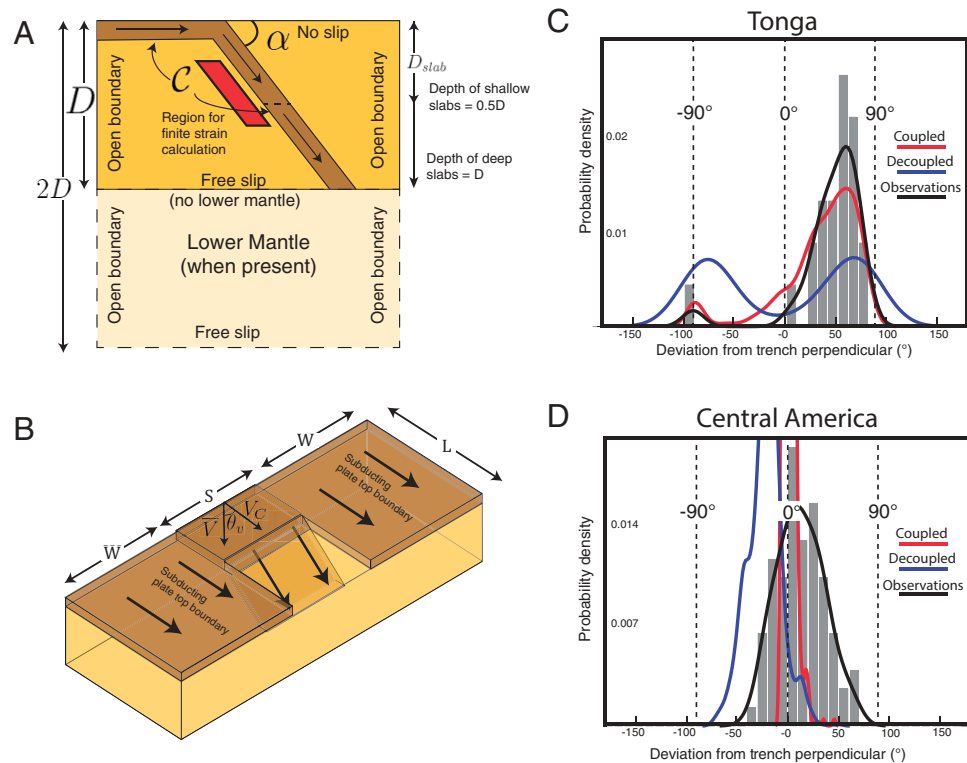


Figure 3. Model setup and predicted finite strain ellipsoid (FSE) orientations modified from Paczkowski et al. (2014b). (A) 2D view and (B) 3D view of Paczkowski et al. (2014b) models used in this study. Values for slab dip, α ; depth of the subducting plate, D_{slab} ; coupling factor, C ; depth of the upper mantle and lower mantle, D ; convergence velocity, V_c ; background mantle flow, V and Θ ; and the boundary conditions are shown. (C) Predicted FSE orientations for coupled (red) and uncoupled (blue) Tonga models. Orientations are shown relative to the trench geometry such that 0° corresponds to trench-perpendicular. Observed fast-splitting orientations are shown in histogram and as a smoothed distribution (black). (D) Predicted FSE orientations for the Central America model plotted following the same conventions as (C).

In order to evaluate their models, Paczkowski et al. (2014b) calculated FSEs by integrating the velocity gradient field along a series of streamlines in the modeled sub-slab mantle to compare against observations of shear-wave splitting. The modeled sub-slab mantle corresponds to the volume from 160 km to 435 km depth and ranging from 67 km to 200 km in distance from the slab. The sub-slab region extends 670 km parallel to the trench strike. In total, 1331 individual FSEs populate the sub-slab mantle (Paczowski et al., 2014b). In the majority of subduction zones considered, the FSEs generally align with observed fast directions. However, as discussed above, a direct comparison of FSEs with splitting measurements involves significant simplifying approximations.

While the majority of subduction parameters in the Paczkowski et al. (2014a) models were chosen to be consistent with real world subduction zones, all of the modeled subducting slabs are perfectly planar. For this reason, we have chosen to restrict our examination of sub-slab anisotropy in this study to the models for Tonga and Central America, which both have relatively straight slabs. Although regions such as the Aleutians or Sumatra are well sampled observationally, they are characterized by long, curved trenches. The ~1000-km-wide slabs employed in the models are an imperfect analogue to these regions.

In the geodynamic models, the kinematically defined Tonga slab is characterized by a 60° dip, nearly trench perpendicular plate motion, and a slab depth that reaches the lower mantle. In this model, the sub-slab mantle has been decoupled from the downgoing slab, resulting in 3D return flow in the sub-slab mantle (Fig. 4). In the model for Central America, the kinematically defined slab has a dip of 56° , stops at 335 km depth, and has a nearly trench-perpendicular plate motion. The sub-slab mantle is fully coupled to the subducting slab, resulting in entrained flow (Fig. 5). Each model approximates one of the two end-member flow regimes—3D return flow and entrained flow.

2.3 Shear-Wave Splitting Data Set

The source-side splitting observations for the Tonga and Central American subduction zones come from the studies of Foley and Long (2011) and Lynner and Long (2014a), respectively. Source-side, shear-wave splitting is a powerful tool to examine anisotropy beneath a seismic source, such as earthquakes associated with subduction. By first constraining and then

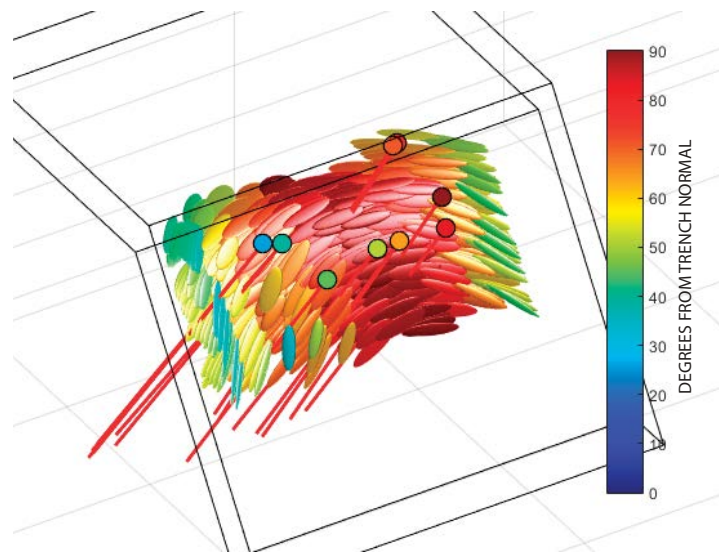


Figure 4. Finite strain ellipsoids (FSEs) for the Tonga model from Paczkowski et al. (2014b). The color of each FSE is the absolute deviation of the maximum-stretch azimuth from the trench-normal azimuth. Rays (red lines) are plotted from their source (circles) to the upper mantle at the bottom of the model. The colors of the circles denote an individual ray. These identifying colors are maintained through subsequent Figures 8, 10, and 11.

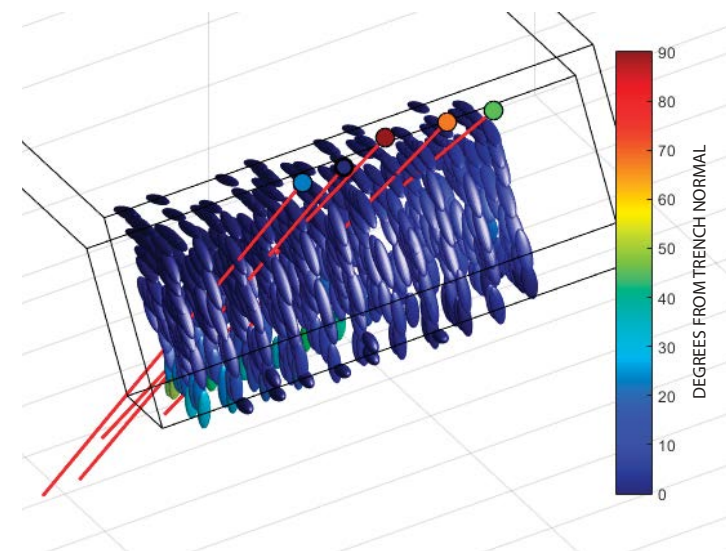


Figure 5. Finite strain ellipsoids (FSEs) for the Central America model are from Paczkowski et al. (2014b). Plotting conventions are as in Figure 4. The colors of the circles denote an individual ray. These identifying colors are maintained through subsequent Figures 9, 10, and 11.

removing anisotropy beneath a seismic station, we can directly measure shear-wave splitting originating in the sub-slab mantle (see Lynner and Long [2014a] for additional discussion of source-side, shear-wave splitting techniques and receiver-side anisotropy corrections). Tonga source-side measurements were made at seismic stations in the southwestern United States and the Baja Peninsula. Source-side observations for Central America were recorded at stations in the Pacific Northwest, Alaska, and South America. Signal contamination from anisotropy within the slab itself can cause variations in the observed splitting and obscure the signal of anisotropy from the sub-slab mantle; therefore, station locations were chosen to minimize the amount of slab sampled by the S waves. As a test of potential slab contributions to the observed source-side signal, Lynner and Long (2014a) compared splitting observations from rays with varying slab path lengths and concluded that anisotropy within the slabs themselves was negligible in their data set. Initial shear-wave polarization was calculated using the SplitLab software package of Wüstefeld et al. (2008) for each measurement.

In Tonga, the average source-side splitting delay time is ~ 1.2 s with fast directions that are parallel to subparallel to trench strike (Foley and Long, 2011). Beneath Central America, the average delay time is ~ 1.6 s with fast directions that are roughly trench orthogonal. In order to properly assimilate the shear-wave splitting observations into the geodynamic models, we restrict

the source-side measurements used in this study to a subset of the Tonga and Central American data sets, as discussed below. The source-side splitting observations used in this study are shown in Figure 6.

3. METHODS

We compare observations of source-side splitting with predictions calculated from the two regionally specific geodynamic models for each of the five fabric types (A-type, C-type, E-type, the hexagonal approximation, and SRA) shown in Figure 1. An elastically anisotropic volume is generated within the sub-slab model volume by aligning the elastic tensors in each model cell using the maximum, intermediate, and minimum stretch directions calculated by Paczkowski et al. (2014b). The different elastic tensors are oriented such that in each model cell, the finite shear direction associated with each tensor is aligned with the orientation of maximum stretch and the shear-plane normal direction is aligned with the orientation of minimum stretch.

We calculate ray paths through the sub-slab model volume that approximate the ray paths from the observations. Observed rays are translated into the reference frame of the geodynamic models using event depth and event location relative to the edge of the subducting slab (relative to the northern

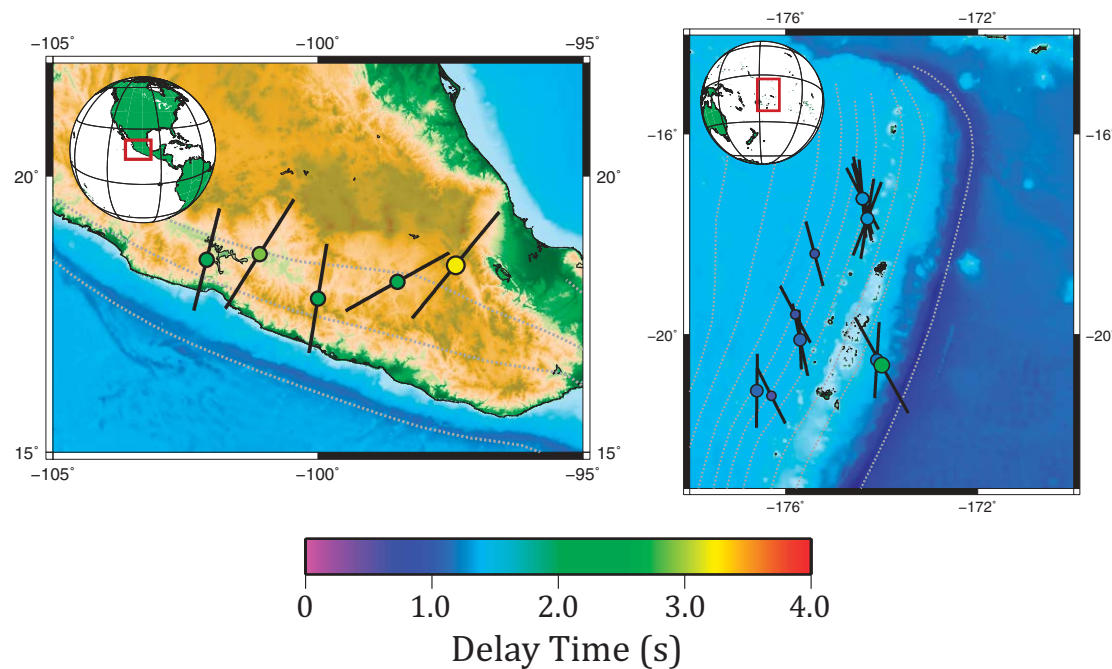


Figure 6. Source-side, shear-wave splitting measurements used in this study from Tonga (right) and Central America (left). The orientation and length of the bars correspond to fast direction and delay time, respectively. Circles are plotted at event locations and denote delay time. For events that yielded multiple observations, only the circle corresponding to the largest delay time is shown.

and western slab edges for Tonga and Central America, respectively). We trace the rays from the source location to a depth of 410 km using TauP (Crotwell et al., 1999) and the iasp91 reference model (Kennett and Engdahl, 1991) (Figs. 4 and 5). We restrict our analysis to rays that sample the portion of the sub-slab mantle where FSEs were calculated. Measurements associated with rays that travel primarily within the modeled slabs and do not primarily sample modeled sub-slab material are excluded. This data selection step is needed because in actual subduction zones, slab dips vary with depth; this allows some rays to travel near the slab (along strike) while still primarily sampling sub-slab mantle material. For the modeled slabs, where a single slab dip is prescribed, these same rays rarely or never leave the slab to sample the sub-slab mantle, and thus we exclude them from our comparison. This problem is particularly acute in Central America, where a large number of the published observations fall into this category.

In Tonga, we restrict our analysis to rays associated with events north of 21.5°S. This choice is necessary in order to compare the modeled and observed splitting because of ~1000-km-wide slabs used in the underlying models. The model slabs in the Paczkowski et al. (2014b) study are only ~1000 km wide; this

choice was made to minimize the effects of the sides of the model domain and slab edges on the predicted flow field and allowed for consistent comparison amongst the different models. Rays sampling the model south of 21.5°S sample a portion of the flow field associated with return flow around the southern edge of the slab. In the real world, those observations are still more than 2000 km away from the southern edge of the slab. We therefore restrict our analysis to the northern portion of the Tonga model, where the analogy between the model slab geometry and the actual slab geometry is valid. While this restricts the number of potential observations against which to compare predicted splitting, it captures the region of highest interest (the region of return flow at the edge of the slab) and still encompasses a majority of available observations for Tonga.

We predict shear-wave splitting for each ray for each anisotropic fabric by tracing each ray through the modeled sub-slab mantle, tracking the elastic tensor and distance traveled in each cell. Using the MSAT software package of Walker and Wookey (2012), we calculate the splitting (fast direction and delay time) predicted for each cell by solving the Christoffel equation for the appropriate elastic tensor. We then calculate the total splitting each ray encounters as a multi-layered volume through a series of two-layered splitting

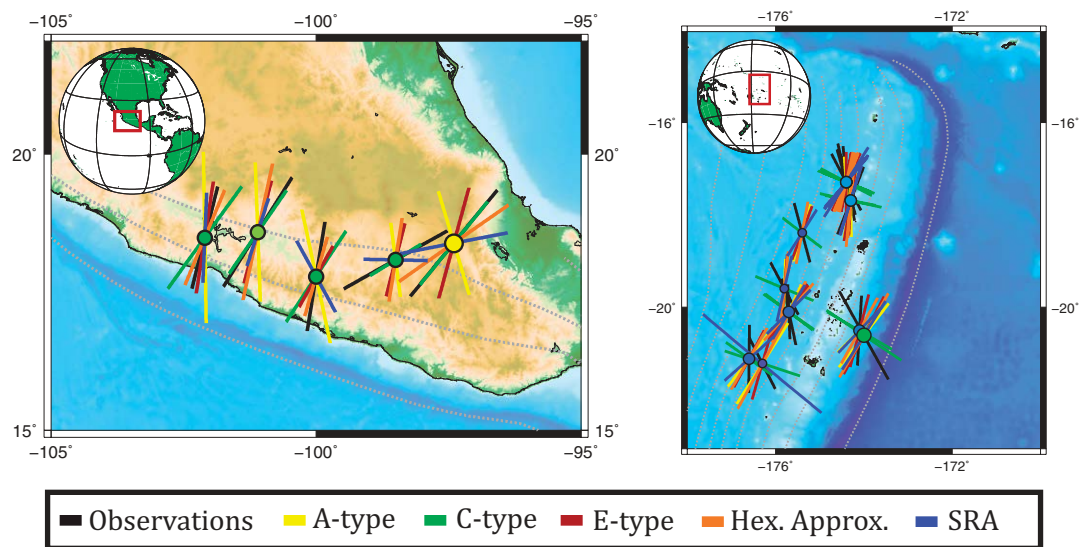


Figure 7. Observed (black) and predicted (colors) shear-wave splitting at Tonga (right) and Central America (left). Colors correspond to fabric types as follows: A-type—yellow; C-type—green; E-type—red; hexagonal (Hex.) approximation—light blue; strong radial anisotropy model (SRA)—dark blue. Circles are plotted at event location and denote delay time of the observation. The length and orientation of the bars represent delay time and fast direction, respectively.

calculations. For each model cell encountered by a ray, we treat the calculated apparent splitting accrued to that point and the splitting due to the model cell as two distinct layers. We then calculate a new apparent splitting including both layers. This is repeated for every model cell encountered until the ray exits the sub-slab mantle.

4. RESULTS

The predicted shear-wave splitting patterns for all five candidate anisotropic fabrics for both the Tonga and Central America subduction models can be seen in map view in Figure 7 and plotted as a function of initial polarization in Figures 8 and 9, respectively. In Tonga, observed fast-splitting directions are generally trench parallel to subparallel. Most candidate fabrics correctly predict trench-parallel, fast-splitting directions. Specifically, A-type, E-type, the hexagonal approximation, and the SRA fabrics all predict roughly trench-parallel fast directions; only the C-type olivine fabric predicts non-trench-parallel orientations. Of those fabrics that predict roughly trench-parallel splitting, A-type and strong radial fabrics show the largest spread (variance in predicted splitting parameters) in fast directions, and all four show greater than 1 s spread in predicted delay times. For the Central America model, where observations are generally trench orthogonal, all five fabrics predict roughly trench-orthogonal fast directions and have a >1 s spread in delay times.

In addition to individual comparison between predicted and observed splitting, a useful observation is the overall spread in predicted fast directions. For

both Central America and Tonga, there is minimal spread in observed fast-splitting directions because most observations are within $\sim 35^\circ$ and $\sim 20^\circ$ of each other, respectively (Foley and Long, 2011; Lynner and Long, 2014a). We can use the spread of the predicted splitting for each ray path over all possible initial polarizations (gray lines in Figs. 8 and 9) as a semiquantitative way to evaluate the predictions for different fabrics. Fabrics that exhibit large variability in splitting behavior over a wide range of initial polarizations would likely show significantly more spread in predicted fast directions than is actually observed. In both Central America and Tonga, a fairly wide range of initial polarizations are represented in the observations (Lynner and Long, 2014a); yet the level of spread in the observed fast-splitting directions is far less than that predicted in the highly variable regions shown in Figures 8 and 9. In the Tonga model, A-type and SRA fabrics exhibit significant variability in splitting over much wider ranges of initial polarization than the hexagonal approximation or E-type fabrics (Fig. 8). The relatively small range of initial polarization values over which splitting varies significantly in the predictions for the E-type and the hexagonal approximation fabrics suggests they are more likely candidates for the sub-slab mantle in this region. Comparing the spread in splitting over initial polarization is less useful for the Central America model (Fig. 9) because there are fewer suitable observations. Still, it is apparent that C-type fabric has the smallest range in initial polarizations over which predicted fast directions are highly variable.

In our comparisons between observed and predicted shear-wave splitting, we choose to focus on fast direction rather than delay time. Observationally, delay times are less well constrained than fast directions, with larger errors. Additionally, when modeling splitting, changing the strength of anisotropy

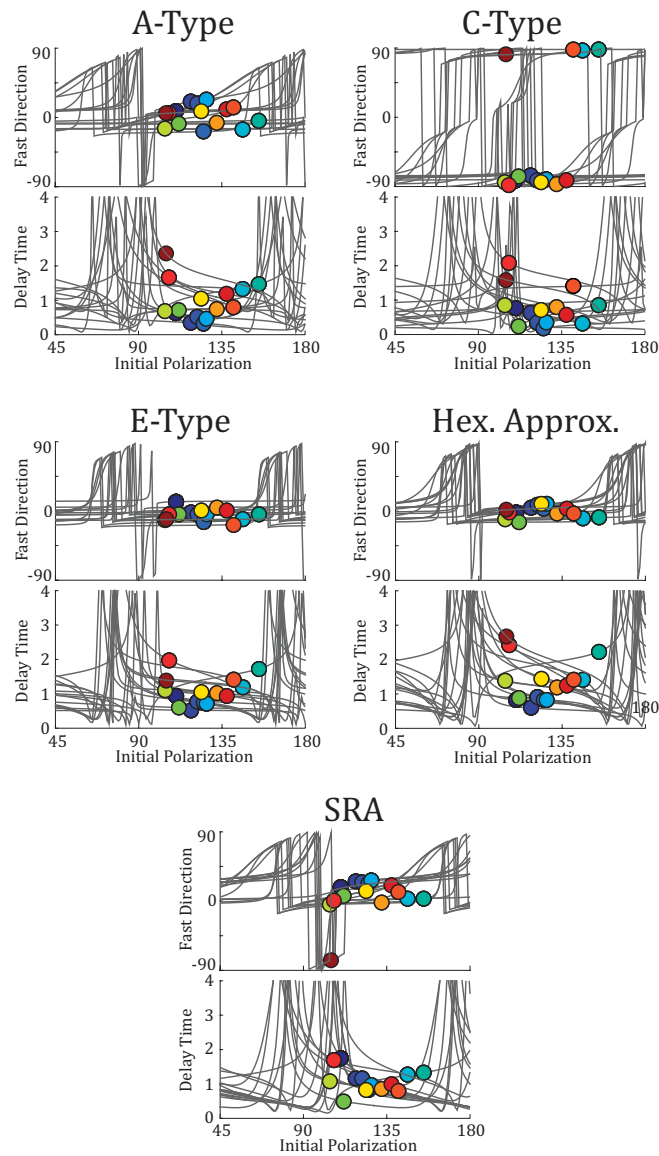


Figure 8. Splitting predictions for five candidate anisotropic fabric scenarios for the Tonga flow model plotted as a function of initial polarization. Colored circles denote predicted splitting for the observed initial polarization of each ray, with the colors corresponding to the rays as identified in Figure 4. Gray lines show predicted splitting of each ray across all possible initial polarizations. Fast directions are oriented relative to the strike of the trench with 0° being trench parallel. SRA—strong radial anisotropy model.

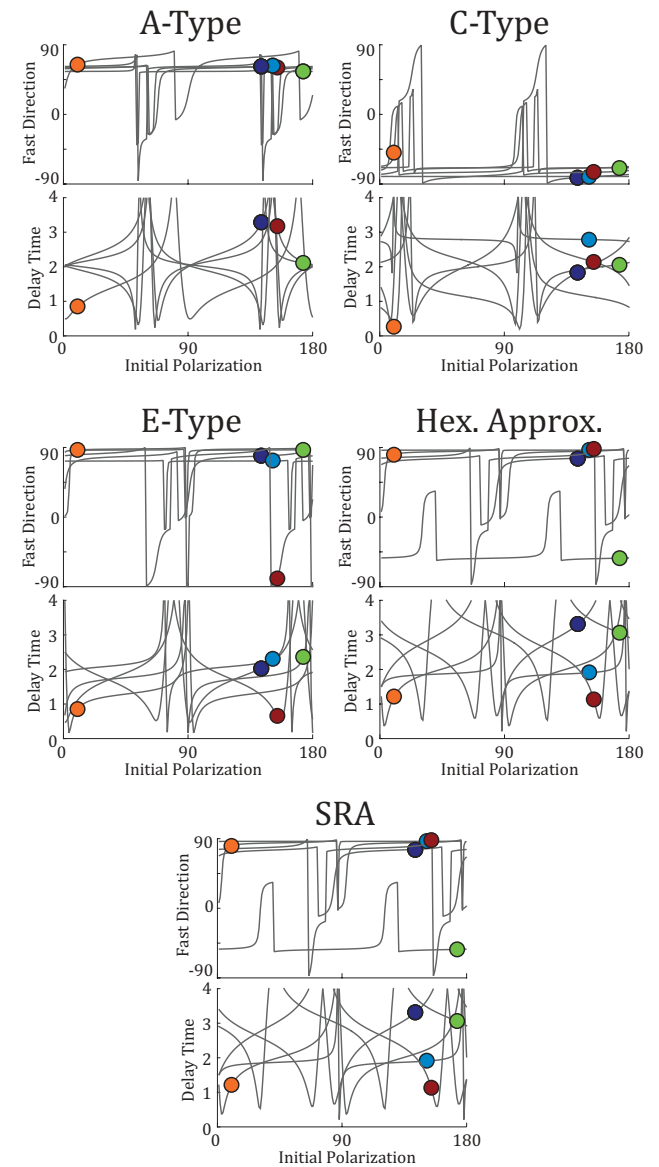


Figure 9. Splitting predictions for Central America, following the same plotting conventions as in Figure 8. Colors correspond to the ray geometries identified in Figure 5. SRA—strong radial anisotropy model.

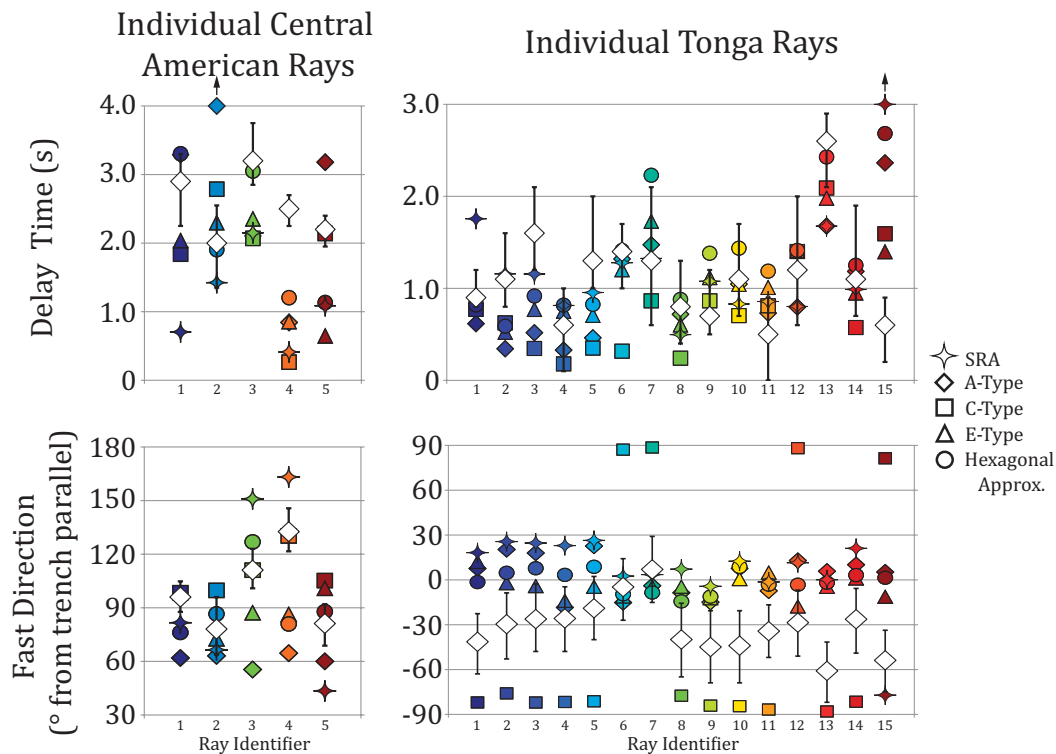


Figure 10. Predicted delay times (top) and fast directions (bottom) for the five candidate fabric types (colored symbols). Colored symbols correspond to individual rays as identified in Figures 4 and 5. Observed shear-wave splitting measurements are plotted (open diamonds) along with their corresponding 2σ error bars. Fast directions for both the predicted and observed splitting are in the model reference frame. SRA—strong radial anisotropy model.

and layer thickness strongly affects delay-time predictions. In this study, we use the strength of anisotropy prescribed by each tensor, but we restrict the volume of sub-slab mantle to the region within 200 km of the slab. This reasonable but arbitrary choice of layer thickness means that the delay-time predictions are less meaningful than those for fast directions. For these reasons, in our ensuing discussion of the best-fitting fabrics for each model, we focus on predictions of fast direction.

Figure 10 shows the predicted splitting parameters for each fabric type along with the corresponding observation and 2σ error (as calculated by the SplitLab software package; Wüstefeld et al., 2008), while Figure 11 shows the deviation between observed and predicted splitting. Comparing predictions and observations reveals that for Tonga, E-type fabric provides the best overall match to the observations in both fast direction and delay time. In Central America, C-type fabric provides the best fit for fast direction, while the hexagonal approximation fabric best matches delay time. For the Tonga model, while E-type fabric best

fits the data, the A-type and hexagonal olivine LPO approximation fabrics also match well, and we cannot distinguish statistically among them (using a two-tailed t-test at $p < 0.05$). In Tonga, only C-type fabric is a statistically worse fit than E-type fabric. For the Central America model, C-type fabric provides the best fit to the observations and is a much better fit than any other anisotropic fabric (Figs. 10 and 11). Again, however, given the limited number of observations, it is not possible to distinguish statistically among the best-fitting fabrics.

5. DISCUSSION

Using the 3D flow models of Paczkowski et al. (2014a, 2014b), the anisotropy scenario that best fits the observations in Tonga is E-type fabric; notably, the C-type fabric predicts a poor fit to the observations. Beneath Central America, in contrast, the best-fitting anisotropy scenario is the C-type fabric. In both

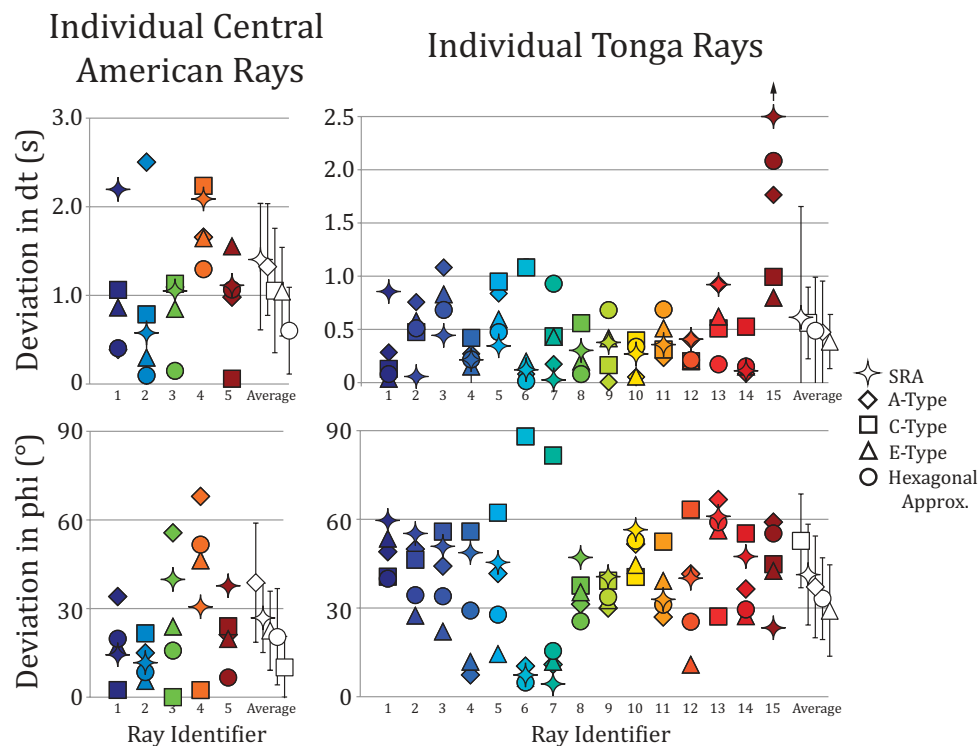


Figure 11. Comparison of deviations in delay times (top) and fast-splitting directions (bottom) for each of the five fabric types and the observed source-side, fast-splitting directions for each individual ray, for Tonga (right) and Central America (left). Open symbols denote the regionally averaged deviation associated with each fabric type. Colored symbols correspond to individual rays as shown in Figures 4 and 5. Error bars representing one standard deviation of the difference between observed and predicted splitting are plotted for the fabric averages. SRA—strong radial anisotropy model. Approx.

cases, there was substantial variability in splitting predictions resulting from different fabric choices. This finding highlights the limitations of the Lynner and Long (2014b) study and other geodynamic modeling studies that do not take into account different LPO fabric types. When we consider the 3D flow models used in this study, we find that the hexagonal approximation to olivine LPO elasticity does not provide the best fit to the observations in either region. This illustrates the need to consider a range of olivine fabric scenarios when comparing predictions from geodynamic models to observations of shear-wave splitting. We note, however, that in both regions the hexagonal approximation fabric is the second best-fitting fabric, suggesting it captures a significant portion of the anisotropic signal from various olivine LPO fabrics. The hexagonal approximation therefore remains a good choice when information about more likely fabrics is lacking.

What can our results tell us about the appropriateness of the 2D simplifications in sub-slab flow employed by the earlier study of Lynner and Long (2014b)? In Tonga, where 3D return flow dominates in the numerical models, we find that the hexagonal olivine LPO approximation fits the data less well than in the simplified study of Lynner and Long (2014b). Specifically, Lynner and Long (2014b) found an average deviation between the predictions and

observations of $\sim 29^\circ$, compared to $\sim 33^\circ$ in this study. This difference, however, is not statistically significant. This nonetheless suggests that while the simplifying assumption of uniformly trench-parallel anisotropy used by Lynner and Long (2014b) managed to capture some aspects of the 3D flow field, the approximation was imperfect. In Central America, where entrained flow dominates, the hexagonal olivine LPO approximation fabric offers a very similar fit to the simplified approximation of Lynner and Long (2014b) (average deviations of $\sim 20^\circ$ and $\sim 22^\circ$, respectively). The simplified assumption that anisotropy aligns locally with the motion of the downgoing slab therefore seems to have sufficiently captured the features of entrained flow.

We find that for both study areas, different candidate anisotropic fabrics predict noticeably different splitting (Figs. 10 and 11). The reason for this can be seen in Figure 1, which shows splitting predictions over a range of initial polarizations and incidence angles for the five different anisotropic fabrics tested in this study. While all five fabrics predict a range of ray-path orientations (initial polarization and azimuth) for which fast-splitting directions are oriented parallel to the shear direction (e.g., for the nearly vertical incidence associated with SK(K)S phases), several orientations exist for which fast-splitting directions deviate significantly from the shear direction. Even the hexagonal approximation

of olivine LPO (a perfectly hexagonal elastic tensor) predicts differences between the shear direction and fast-splitting directions for a wide range of initial polarizations and incidences. This dependence on ray-propagation direction for the various anisotropic fabrics demonstrates the need to consider the details of various candidate fabrics in order to accurately compare geodynamic models and observations of shear-wave splitting.

Hydration state plays a primary role in controlling fabric development in the mantle, with C-type or E-type LPO fabric developing at different water contents (Karato et al., 2008). Taken at face value, then, our results suggest that the sub-slab mantle beneath Central America may be more hydrated than the mantle beneath the Tonga, because C-type fabric is associated with higher water contents than E-type (greater than and less than ~700 ppm H/Si, respectively). While E-type fabric predicts only a slightly better fit to the Tonga source-side splitting measurements than most of the other candidate fabrics, it does provide a statistically better fit than C-type LPO. In contrast, beneath Central America, C-type fabric provides the best fit to the data. Our inference of variable sub-slab mantle water content, if borne out by future investigations, has several implications on both regional and global scales. For example, it may suggest lower viscosity mantle beneath Central America, which would affect the regional dynamics; on a global scale, variations in sub-slab water content would affect the overall budget of water transport into the lower mantle. While there are few independent constraints on spatial variations in the hydration state of the mantle against which to test this assertion, and a mechanism for varying mantle water content is not immediately clear, the suggestion that the sub-slab mantle beneath Central America may be more hydrated than that beneath Tonga provides an interesting target for future study.

Alternatively, the fabric in one or both locations may not directly reflect the FSEs. Laboratory experiments and numerical simulations show that the initial fabric of a deforming aggregate influences olivine LPO even for shear strains as high as 3 (Boneh and Skemer, 2014; Boneh et al., 2015). An additional complication is the presence of coaxial deformation (that is, pure shear as opposed to simple shear) in the models, which is not accounted for in our choice of fabric types based on experiments in simple shear geometry. Furthermore, the different relative amounts of coaxial and non-coaxial deformation in Tonga and Central America may in principle result in different LPO development even if the fabric type is identical. In the geodynamic models that underlie our study, sub-slab deformation in Central America has a larger non-coaxial deformation component than in Tonga. This is shown in Figure 12, both by the kinematic vorticity number, W_k (Truesdell, 1954; Means et al., 1980), and the internal rotation angle. W_k is a ratio of the rate of rotation over the rate of stretching, such that W_k is 0 for coaxial deformation (pure shear), and W_k equals 1 for non-coaxial deformation (simple shear). Internal rotation angle refers to the total rotation of the principal axis of the strain ellipsoid. This angle increases with increasing shear strain (non-coaxial deformation). Both metrics highlight that the Central America model deforms primarily via non-coaxial deformation, while in Tonga, coaxial deformation dominates. More advanced models

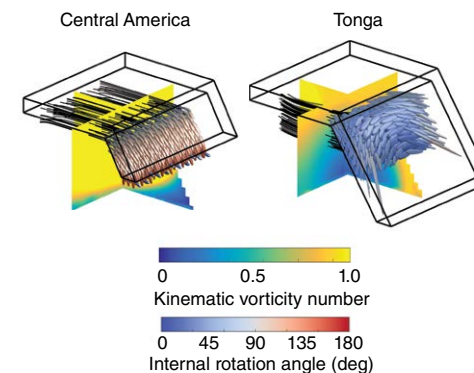


Figure 12. Kinematic vorticity (background) and internal rotation angles (colored finite strain ellipsoids [FSEs]) for the Tonga (right) and Central America (left) models. Both quantities characterize the amount of coaxial and non-coaxial deformation. Non-coaxial deformation manifests in high internal rotation angles and large kinematic vorticity values as seen in Central America, while low values are indicative of coaxial deformation such as in Tonga.

of fabric development are needed to address these complications, and this represents an important target for future work. Available LPO modeling methods (Tommasi et al., 2000; Kaminski et al., 2004) are, however, limited with respect to the range of fabric type that they can reproduce.

There may be other anisotropic fabrics not tested in this study that would better match the observations. The average deviation between observed and predicted fast-splitting directions for E-type LPO for the Tonga flow model, for example, is fairly large at ~29°. Contributions from other mineral phases likely contribute to sub-slab anisotropy and may account for the imperfect match between the predictions of our preferred models and the observations. Factors such as the effect of secondary phases, deformation in polyphase aggregates, and the influence of preexisting fabrics must be better constrained and understood in order to take full advantage of shear-wave splitting observations as data sets against which to test geodynamic models.

Another potential limitation is that the dynamics of the sub-slab mantle are likely imperfectly captured by the numerical models; this may be an additional factor in the misfits between observed and predicted splitting. While the model parameters were all chosen to best mimic those observed in Central America and Tonga, including present-day rollback rates, there are several reductive assumptions made in the models. In particular, all of the models assume instantaneous flow fields, which do not capture temporal variability in dynamics. Therefore, any transient signal due to time-varying tectonic events may be missed. Additionally, any variations in along-strike trench rollback limit the application of our geodynamic models. These potential pitfalls seem to be less problematic in Central America, where splitting associated with C-type fabric fits the data well; however, for Central America, there are limitations on the observational side. Only a handful of published

splitting measurements are associated with ray paths that provide an appropriate comparison to the model results. Additional source-side splitting measurements in that region are necessary to fully assess the range of LPO fabric scenarios.

6. SUMMARY

We present comparisons between observations of shear-wave splitting and predictions from 3D numerical geodynamic models that approximate subduction beneath Tonga and Central America. We employ a range of candidate anisotropic fabric scenarios to compare against observations of sub-slab shear-wave splitting. We show that predicted shear-wave splitting can vary a great deal for identical geodynamic models when different anisotropic fabrics are used. Beneath Tonga, we find that E-type olivine LPO fabric provides the best fit to observations. Other candidate fabrics, except for C-type olivine, provide a statistically similar fit to the observations. Beneath Central America, C-type fabric provides the best fit to the data. These results demonstrate that when carrying out comparisons between geodynamic models and observations of shear-wave splitting, the choice of anisotropic fabric is a key factor. Our results also suggest that a single LPO fabric is not universally present in the upper mantle. Because water content is a major controlling factor in LPO fabric development, the mantle beneath the subducting slab in Central America may be more hydrated than that beneath Tonga. To test this hypothesis, further work is needed such as more realistic simulations of texture development for a range of fabric types, more realistic geodynamic models that include fully dynamic slabs and more realistic slab morphologies, and additional shear-wave splitting observations.

ACKNOWLEDGMENTS

Several figures in the study were prepared using the Generic Mapping Tools (Wessel and Smith, 1991). We thank Erin Wirth and Christopher McKitterick for comments on this manuscript. Thoughtful comments by two anonymous reviewers helped us to improve the presentation of the material. This work was funded by National Science Foundation grant EAR-1150722.

REFERENCES CITED

- Abt, D.L., Fischer, K.M., Abers, G.A., Protti, M., González, V., and Strauch, W., 2010, Constraints on upper mantle anisotropy surrounding the Cocos slab from SK(K)S splitting: *Journal of Geophysical Research*, v. 115, B06316, doi:10.1029/2009JB006710.
- Boneh, Y., and Skemer, P., 2014, The effect of deformation history on the evolution of olivine CPO: *Earth and Planetary Science Letters*, v. 406, p. 213–222, doi:10.1016/j.epsl.2014.09.018.
- Boneh, Y., Morales, L.F.G., Kaminski, E., and Skemer, P., 2015, Modeling olivine CPO evolution with complex deformation histories: Implications for the interpretation of seismic anisotropy in the mantle: *Geochemistry, Geophysics, Geosystems*, v. 16, no. 10, p. 3436–3455, doi:10.1002/2015GC005964.
- Chevrot, S., and van der Hilst, R.D., 2003, On the effects of a dipping axis of symmetry on shear wave splitting measurements in a transversely isotropic medium: *Geophysical Journal International*, v. 152, p. 497–505, doi:10.1046/j.1365-246X.2003.01865.x.
- Conrad, C.P., and Behn, M.D., 2010, Constraints on lithosphere net rotation and asthenospheric viscosity from global mantle flow models and seismic anisotropy: *Geochemistry, Geophysics, Geosystems*, v. 11, Q05W05, doi:10.1029/2009GC002970.
- Crampin, S., and Peacock, S., 2008, A review of the current understanding of seismic shear-wave splitting in the Earth's crust and common fallacies in interpretation: *Wave Motion*, v. 45, no. 6, p. 675–722, doi:10.1016/j.wavemoti.2008.01.003.
- Crotwell, H.P., Owens, T.J., and Ritsema, J., 1999, The TauP Toolkit: Flexible seismic travel-time and ray-path utilities: *Seismological Research Letters*, v. 70, p. 154–160, doi:10.1785/gssrl.70.2.154.
- DeMets, C., Gordon, R.G., Argus, D.F., and Stein, S., 1994, Effect of recent revisions to the geomagnetic reversal time scale on estimates of current plate motions: *Geophysical Research Letters*, v. 21, no. 20, p. 2191–2194, doi:10.1029/94GL02118.
- Di Leo, J., Walker, A., Li, Z.-H., Wookey, J., Ribe, N., Kendall, J.-M., and Tommasi, A., 2014, Development of texture and seismic anisotropy during the onset of subduction: *Geochemistry, Geophysics, Geosystems*, v. 15, p. 192–212, doi:10.1002/2013GC005032.
- Faccenda, M., and Capitanio, F.A., 2012, Development of mantle seismic anisotropy during subduction-induced 3-D flow: *Geophysical Research Letters*, v. 39, L11305, doi:10.1029/2012GL051988.
- Faccenda, M., and Capitanio, F.A., 2013, Seismic anisotropy around subduction zones: Insights from three-dimensional modeling of upper mantle deformation and SKS splitting calculations: *Geochemistry, Geophysics, Geosystems*, v. 14, p. 243–262, doi:10.1002/ggge.20055.
- Foley, B.J., and Long, M.D., 2011, Upper and mid-mantle anisotropy beneath the Tonga slab: *Geophysical Research Letters*, v. 38, no. 2, L02303, doi:10.1029/2010GL046021.
- Jadamec, M., and Billen, M., 2010, Reconciling surface plate motion and rapid three-dimensional flow around a slab edge: *Nature*, v. 465, p. 338–341, doi:10.1038/nature09053.
- Jung, H., Katayama, I., Jiang, Z., Hiraga, T., and Karato, S., 2006, Effect of water and stress on the lattice-preferred orientation of olivine: *Tectonophysics*, v. 421, p. 1–22, doi:10.1016/j.tecto.2006.02.011.
- Kaminski, É., Ribe, N.M., and Browaeys, J.T., 2004, D-Rex, a program for calculation of seismic anisotropy due to crystal lattice preferred orientation in the convective upper mantle: *Geophysical Journal International*, v. 158, p. 744–752, doi:10.1111/j.1365-246X.2004.02308.x.
- Karato, S., 2012, *Deformation of Earth Materials: An Introduction to the Rheology of Solid Earth*: Cambridge, UK, Cambridge University Press, 463 p.
- Karato, S., Jung, H., Katayama, I., and Skemer, P., 2008, Geodynamic significance of seismic anisotropy of the upper mantle: New insights from laboratory studies: *Annual Review of Earth and Planetary Sciences*, v. 36, p. 59–95, doi:10.1146/annurev.earth.36.031207.124120.
- Kennett, B.L.N., and Engdahl, E.R., 1991, Traveltimes for global earthquake location and phase identification: *Geophysical Journal International*, v. 105, p. 429–465, doi:10.1111/j.1365-246X.1991.tb06724.x.
- Kneller, E., and van Keken, P., 2007, Trench-parallel flow and seismic anisotropy in the Mariana and Andean subduction systems: *Nature*, v. 450, p. 1222–1225, doi:10.1038/nature06429.
- Korenaga, J., and Jordan, T.H., 2003, Physics of multiscale convection in Earth's mantle: Onset of sublithospheric convection: *Journal of Geophysical Research*, v. 108, no. B7, 2333, doi:10.1029/2002JB001760.
- Kumazawa, M., and Anderson, O.L., 1969, Elastic moduli, pressure derivatives, and temperature derivatives of single-crystal olivine and single-crystal forsterite: *Journal of Geophysical Research*, v. 74, no. 25, p. 5961–5972, doi:10.1029/JB074i025p05961.
- Lallemant, S., Heuret, A., and Boutelier, D., 2005, On the relationships between slab dip, back-arc stress, upper plate absolute motion, and crustal nature in subduction zones: *Geochemistry, Geophysics, Geosystems*, v. 6, no. 9, Q09006, doi:10.1029/2005GC000917.
- Li, Z.-H., Di Leo, J.F., and Ribe, N.M., 2014, Subduction-induced mantle flow, finite strain, and seismic anisotropy: Numerical modeling: *Journal of Geophysical Research*, v. 119, p. 5052–5076, doi:10.1002/2014JB010996.
- Long, M.D., 2013, Constraints on subduction geodynamics from seismic anisotropy: *Reviews of Geophysics*, v. 51, p. 76–112, doi:10.1002/rog.20008.
- Long, M.D., and Silver, P.G., 2008, The subduction zone flow field from seismic anisotropy: A global view: *Science*, v. 319, p. 315–318, doi:10.1126/science.1150809.
- Long, M.D., and Silver, P.G., 2009, Mantle flow in subduction systems: The sub-slab flow field and implications for mantle dynamics: *Journal of Geophysical Research*, v. 114, B10312, doi:10.1029/2008JB006200.
- Lynner, C., and Long, M.D., 2013, Sub-slab seismic anisotropy and mantle flow beneath the Caribbean and Scotia subduction zones: Effects of slab morphology and kinematics: *Earth and Planetary Science Letters*, v. 361, p. 367–378, doi:10.1016/j.epsl.2012.11.007.

- Lynner, C., and Long, M.D., 2014a, Sub-slab anisotropy beneath the Sumatra and circum-Pacific subduction zones from source-side shear wave splitting observations: *Geochemistry, Geophysics, Geosystems*, v. 15, no. 6, p. 2262–2281, doi:10.1002/2014GC005239.
- Lynner, C., and Long, M.D., 2014b, Testing models of sub-slab anisotropy using a global compilation of source-side shear wave splitting data: *Journal of Geophysical Research*, v. 119, p. 7226–7244, doi:10.1002/2014JB010983.
- Lynner, C., and Long, M.D., 2015, Lateral variability in mid-mantle and transition zone anisotropy beneath South America and the northwest Pacific: *Geophysical Journal International*, v. 201, no. 3, p. 1545–1552, doi:10.1093/gji/ggv099.
- Means, W.D., Hobbs, B.E., Lister, G.S., and Williams, P.F., 1980, Vorticity and non-coaxiality in progressive deformations: *Journal of Structural Geology*, v. 2, no. 3, p. 371–378, doi:10.1016/0191-8141(80)90024-3.
- Michibayashi, K., Mainprice, D., Fujii, A., Uehara, S., Shinkai, Y., Kondo, Y., Ohara, Y., Ishii, T., Fryer, P., Bloomer, S.H., and Ishiwatari, A., 2016, Natural olivine crystal-fabrics in the western Pacific convergence region: A new method to identify fabric type: *Earth and Planetary Science Letters*, v. 443, p. 70–80, doi:10.1016/j.epsl.2016.03.019.
- Müller, C., Bayer, B., Eckstaller, A., and Miller, H., 2008, Mantle flow in the South Sandwich subduction environment from source-side shear wave splitting: *Geophysical Research Letters*, v. 35, L03301, doi:10.1029/2007GL032411.
- Olugboji, T.M., Karato, S., and Park, J., 2013, Structures of the oceanic lithosphere-asthenosphere boundary: Mineral-physics modeling and seismological signatures: *Geochemistry, Geophysics, Geosystems*, v. 14, p. 880–901, doi:10.1002/ggge.20086.
- Paczkowski, K., Montesi, L.G.J., Long, M.D., and Thissen, C.J., 2014a, Three-dimensional flow in the sub-slab mantle: *Geochemistry, Geophysics, Geosystems*, v. 15, p. 3989–4008, doi:10.1002/2014GC005441.
- Paczkowski, K., Thissen, C.J., Long, M.D., and Montesi, L.G.J., 2014b, Deflection of mantle flow beneath subducting slabs and patterns of seismic anisotropy: *Geophysical Research Letters*, v. 41, p. 6734–6742, doi:10.1002/2014GL026091.
- Russo, R.M. and Silver, P.G., 1994, Trench-parallel flow beneath the Nazca plate from seismic anisotropy: *Science*, v. 263, p. 1105–1111, doi:10.1126/science.263.5150.1105.
- Savage, M.K., 1999, Seismic anisotropy and mantle deformation: What have we learned from shear wave splitting?: *Reviews of Geophysics*, v. 37, p. 65–106, doi:10.1029/98RG02075.
- Schellart, W.P., Stegman, D.R., and Freeman, J., 2008, Global trench migration velocities and slab migration induced upper mantle volume fluxes: Constraints to find an Earth reference frame based on minimizing viscous dissipation: *Earth-Science Reviews*, v. 88, p. 118–144, doi:10.1016/j.earscirev.2008.01.005.
- Song, T.-R.A., and Kawakatsu, H., 2012, Subduction of oceanic asthenosphere: Evidence from sub-slab seismic anisotropy: *Geophysical Research Letters*, v. 39, L17301, doi:10.1029/2012GL052639.
- Song, T.-R.A., and Kawakatsu, H., 2013, Subduction of oceanic asthenosphere: A critical appraisal in central Alaska: *Earth and Planetary Science Letters*, v. 367, p. 82–94, doi:10.1016/j.epsl.2013.02.010.
- Tommasi, A., Mainprice, D., Canova, G., and Chastel, Y., 2000, Viscoplastic self-consistent and equilibrium-based modeling of olivine lattice preferred orientations: Implications for the upper mantle seismic anisotropy: *Journal of Geophysical Research*, v. 105, p. 7893–7908, doi:10.1029/1999JB900411.
- Truesdell, C., 1954, *The Kinematics of Vorticity*: Bloomington, Indiana, Indiana University Press, 232 p.
- van Hunen, J., and Čadež, O., 2009, Reduced oceanic seismic anisotropy by small-scale convection: *Earth and Planetary Science Letters*, v. 284, p. 622–629, doi:10.1016/j.epsl.2009.05.034.
- Walker, A., and Wookey, J., 2012, MSAT-A new toolkit for the analysis of elastic and seismic anisotropy: *Computers & Geosciences*, v. 49, p. 81–90, doi:10.1016/j.cageo.2012.05.031.
- Wessel, P., and Smith, W.H.F., 1991, Free software helps map and display data: *Eos (Transactions, American Geophysical Union)*, v. 72, no. 41, p. 441–446, doi:10.1029/90EO00319.
- Wüstefeld, A., Bokelmann, G., Barruol, G., and Zaroli, C., 2008, Splitlab: A shear-wave splitting environment in Matlab: *Computers & Geosciences*, v. 34, p. 515–528, doi:10.1016/j.cageo.2007.08.002.